Local fluctuations and spatial correlations in granular flows under constant-volume quasistatic shear

Ning Guo and Jidong Zhao[*]

Department of Civil and Environmental Engineering, The Hong Kong University of Science and Technology,
Clearwater Bay, Kowloon, Hong Kong
(Received 2 January 2014; published 25 April 2014)

We investigate the local fluctuations in dense granular media subjected to athermal, quasistatic shearing, based on three-dimensional discrete element method simulations. By shearing granular assemblies of different polydispersities under constant-volume constraint, we quantify the characteristics of local structures (in terms of local volume and local anisotropy) and local deformation (using local shear strain and nonaffine displacement). The distribution of the local volume in a granular medium is found unchanged during the entire shearing process, which indicates a constant temperaturelike compactivity for the material. The compactivity is not, however, equilibrated among different particle groups in a polydisperse assembly. The local structures of a disordered granular assembly are inherently anisotropic. The fluctuations in local anisotropy can be well captured by a gamma or mixed-gamma distribution function, which is also unchanged during the shear. The local anisotropic orientation evolves towards the coaxial direction of the stress anisotropy with shear. The deformation characteristics of a jammed granular medium have their origins in the structural amorphousness. The local shear strain field depicts clear shear transformation zones which act as plasticity carriers. The spatial correlation of the local shear strains exhibits a fourfold pattern which is stronger in the stress deviatoric planes than in the stress isotropic plane. The fluctuations of nonaffine displacement suggest an isotropic granular temperature and an isotropic spatial correlation independent of the stress state. Both the local strain and the nonaffine displacement exhibit a power-law decayed distribution with a long-range correlation. We further modify the shear-transformation-zone theory to predict the pressure-dependent constitutive behavior of a sheared granular material and compare its prediction with our simulation data.

I. INTRODUCTION

A granular material may behave either fluid- or solidlike. When subjected to adequate confinement, it can respond like a perfect solid, capable of sustaining remarkable shear with finite strain due to jamming [1–3] where the constituent particles attain sufficient contacts from their neighborhood and behave as if totally caged to lead to rigidity for the entire material body. The short-ranged interparticle contacts, together with the constituent particles and the associated voids, form strongly heterogeneous and amorphous internal structures in the material which underpin complex macroscopic physical and mechanical responses of the material. Quantitative identifications of the characteristics of these local structures and the associated deformations constitute a key step towards demystifying the behavior of granular media.

As an isotropic measure of the local structure, density plays a key role dictating the behavior of granular media. For example, increasing density may lead to a fluid-to-solid phase transition according to the jamming phase diagram [4]. The statistical mechanics theory developed by Edwards employs an effective temperature or compactivity [5] based on the volume (or density) of a microcanonical ensemble to describe the jammed behavior of granular media. The compactivity has recently been related to the local volume fluctuations [6–8]. The deformation of a granular material arises from the local volume fluctuations too, i.e., the free volumes in the material may activate particle rearrangements and cause

plastic deformation. The plastic flow in the material is often governed by clusters of randomly close packed particles which cooperatively reorganize themselves to sustain the applied shear, which differ apparently from that in crystalline solids where dislocations induce plasticity. These plasticity-bearing clusters in granular media are termed as shear transformation zones (STZs) [9–11]. Langer and co-workers [12–15] have indeed developed their shear transformation zone model based on observations of local quantities in a granular medium or an amorphous solid. Local displacement in a granular medium may embody important deformation properties too. It has been observed that the fluctuated (nonaffine) displacements in a granular material may form vortexlike patterns [16,17] and show strong spatial correlations [18,19].

Most existing studies on the local properties of granular media have been focused on specific loading protocols such as simple shear where the material states can be simply described by scalar variables. These simplifications, however, cannot fully reflect the general real three-dimensional nature of practical problems [20]. These studies appear also to be interested in certain specific states of granular media only, such as the stationary state [6,7], the jamming transition state [21,22], or the sheared steady state [23,24]. Examining the evolution of the local quantities during the entire shearing course may offer new insights towards understanding the granular behavior. In this study, we employ a discrete element method (DEM) to perform a series of three-dimensional shearing tests on granular assemblies. Based on the simulation data, we examine the key characteristics of local structures and deformation during the shearing process. While the density has been frequently investigated in the literature, it can only

[*]Corresponding author: jzhao@ust.hk

serve as an isotropic characterization of the local structure. While a granular medium is inherently anisotropic [25], structural anisotropy should be paid more attention toward a comprehensive understanding of the local structure properties, which will be pursued in this study. To exclude the influence of global volume fluctuation, we impose a constant-volume constraint on all assemblies during the shearing process. The constant-volume shearing protocol is indeed common both in laboratory tests [26,27] and numerical simulations [28,29]. In soil mechanics, it may correspond to the so-called undrained shear if the interstitial water is absent. In the deformation analyses, the statistical properties of both the local strain and the nonaffine displacement will be of major interest in our study.

The paper is organized as follows. The simulation details and formulations will be described first, followed by analyses and discussion of the local structures and deformations. The cross correlations among the local quantities will also be discussed. We further modify the STZ model and compare its prediction with our simulation data. For the notations adopted in the study, compression is taken as positive for stress and strain measurements; "⊗," "·," and ":" denote the tensorial dyadic operator, the inner product, and the double contraction, respectively. "tr" and "dev" take the trace and the deviator of a tensor, respectively.

II. METHODOLOGY AND FORMULATIONS

A. Simulations

A three-dimensional DEM code, ESYS-PARTICLE [30], is employed for the study. In the DEM simulations we use spherical particles and a linear force-displacement contact law in conjunction with a Coulomb criterion to describe the frictional stick-slip behavior of interparticle contacts. Three parameters are involved in the contact model: the normal stiffness k_n, the tangential stiffness k_t, and the frictional coefficient μ, based on which the pure-repulsive normal force $\mathbf{f}_n^c$ and the tangential (frictional) force $\mathbf{f}_t^c$ are determined as follows:

$$\mathbf{f}_n^c = -k_n \delta\, \mathbf{n}^c, \tag{1a}$$

$$\mathbf{f}_t^c = \begin{cases} -k_t \mathbf{u}_t^c & \text{if } |\mathbf{f}_t^c| \leqslant \mu|\mathbf{f}_n^c| \quad \text{(sticking)} \\ -\mu|\mathbf{f}_n^c|\, \mathbf{u}_t^c/|\mathbf{u}_t^c| & \text{otherwise} \qquad \text{(slipping)}, \end{cases} \tag{1b}$$

where δ is the overlap of the two contacted particles, $\mathbf{n}^c$ is the outward contact normal, and $\mathbf{u}_t^c$ is the accumulated relative tangential displacement at the contact. We choose the parameters as follows: $k_n/R^* = 10^8$ Pa, where R^* [$=\pi(R_1 + R_2)/4$] is the equivalent radius of the two contacted particles with radii R_1 and R_2, respectively. From Mindlin's analysis on elastic contact, the ratio k_t/k_n is equal to $2(1-\nu)/(2-\nu)$ with ν being the Poisson's ratio of the particle material, which further leads to a relation $2/3 < k_t/k_n < 1$ (see also Ref. [31]) since most materials have $0 < \nu < 1/2$. Hence we set $k_t/k_n = 0.8$ by assuming $\nu = 0.3$, which is appropriate for silica sand particles. We also choose $\mu = 0.5$ for interparticle friction according to the property of silica sand.

We consider four assemblies with different polydispersities as summarized in Table I. The simulation process consists of the following three steps. (a) Assembly generation: We generate the assemblies by randomly inserting particles with

TABLE I. Summary of generated assemblies for the study. MN: monodisperse; BI12/BI21: bidisperse; TRI: tridisperse.

Label	Radii (mm)	ϕ[a]	Proportion[b]
MN	0.25	0.601	NA
BI12	0.2, 0.3	0.605	1:2
BI21	0.2, 0.3	0.611	2:1
TRI	0.2, 0.25, 0.3	0.606	1:1:1

[a]The volume fraction for the monodisperse packing in jammed glassy state is roughly within 0.58–0.64 [25,35].
[b]The proportion is in terms of particle number.

prescribed sizes (or size distributions in the polydisperse cases) into a cubic box confined by six rigid frictionless walls. A total of 40 865 particles are generated for each of the four assemblies. At this stage no particle-particle or particle-wall overlapping is allowed. (b) Isotropic consolidation: We compress the generated assemblies isotropically until a mean pressure $p = 300$ kPa is reached. By assigning a small μ during the compression we are able to prepare samples with relatively high volume fraction ϕ to ensure they are close to the jammed state. (c) Constant-volume shear: We then apply triaxial shear to each assembly by restricting its volume change. Specifically, we continuously apply compression along the y axis of the sample while adjusting the strain rates in the x and z directions according to $\dot{\epsilon}_x = \dot{\epsilon}_z = -\dot{\epsilon}_y/2$, so that the total volume is maintained unchanged (see Fig. 1). The triaxial shear procedure is commonly followed in laboratory experiments as well as numerical simulations in civil and mechanical engineering, and is indeed a pure shearing mode in three dimensions. To ensure quasistatic deformation, the axial compression strain rate $\dot{\epsilon}_y$ is determined from the inertia number $I := \dot{\epsilon}_y \langle 2R \rangle \sqrt{3\rho/p} \leqslant 10^{-3}$ [32], where R is the particle radius, $\langle \cdot \rangle$ denotes the ensemble average, and ρ ($= 2650$ kg/m³) is the particle density. The time step for the DEM computation is chosen $\Delta t < 0.2\sqrt{m_{\min}/k_n}$ to ensure numerical stability where $m_{\min}$ is the mass of the smallest particle. More details about the simulation technique are described in Refs. [33,34].

To evaluate the shearing effect, we measure the modified Péclet number defined by Pe$^* := \sqrt{3}\dot{\epsilon}_y\tau$, where τ is the relaxation time of the assembly which can be estimated from the diffusivity (mean square displacement $\langle \mathbf{u}^2 \rangle$) of the system during a quiescent period after the isotropic compression.
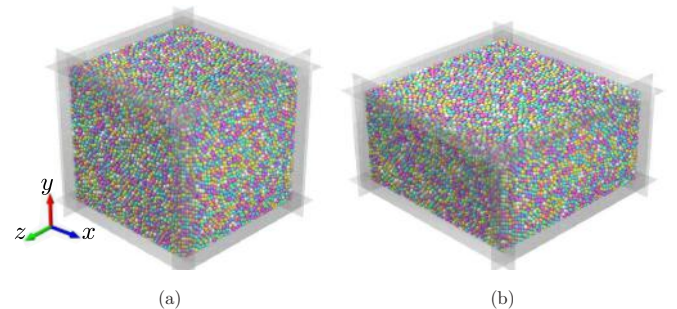

FIG. 1. (Color online) Illustration of constant-volume triaxial shearing: (a) before and (b) after shearing.

While all samples considered here possess a high volume fraction, we have observed extremely low diffusivity and the relaxation time $\tau \propto \langle \mathbf{u}^2 \rangle^{-1} \gg \dot{\epsilon}_y^{-1}$. This leads to $Pe^* \gg 1$, indicating all systems being treated here are athermal and within the shearing dominated regime [36].

B. Macromechanical behavior

The homogenized bulk stress for a discrete assembly can be calculated from the Love formula [37]:

$$\boldsymbol{\sigma} = \frac{1}{V} \sum_{N_c} \mathbf{d}^c \otimes \mathbf{f}^c, \tag{2}$$

where V is the total volume of the assembly, N_c is the number of contacts, $\mathbf{d}^c$ is the branch vector joining the centers of the two contacting particles, and $\mathbf{f}^c$ ($= \mathbf{f}_n^c + \mathbf{f}_t^c$) is the contact force. Based on the stress tensor defined above, the mean stress p and the deviatoric stress q are then calculated as follows:

$$p = \frac{1}{3} \mathrm{tr}\, \boldsymbol{\sigma}, \tag{3a}$$

$$q = \sqrt{\frac{3}{2} \boldsymbol{\sigma}^{\mathrm{dev}} : \boldsymbol{\sigma}^{\mathrm{dev}}}, \tag{3b}$$

where $\boldsymbol{\sigma}^{\mathrm{dev}}$ ($= \mathrm{dev}\, \boldsymbol{\sigma}$) is the deviatoric stress tensor.

The macroscopic mechanical responses of the four assemblies during the shearing are plotted in Fig. 2. With close initial conditions, all assemblies exhibit similar shear behaviors. Evidently, these assemblies can be regarded as dense samples in *soil mechanics*, as they undergo continuous dilation before reaching a final steady state at around $\epsilon_y = 40\%$, after which both p and q stay largely constant. Note that Demkowicz and Argon [38–40] also investigated similar constant-volume plane strain tests on simulated amorphous silicon for both dense and loose samples.

C. Local structure

The local structure of the granular assembly is quantified based on radical Voronoi tessellation (or so-called Laguerre tessellation). This tessellation technique is generalized from the conventional Voronoi tessellation by replacing the bisecting plane with the radical plane, which renders it applicable for

FIG. 2. (Color online) Stress evolution of the four assemblies under constant-volume triaxial shearing. The inset is a zoom-in at small strains, where the star marks the initial yield point.

polydisperse assembly of spheres. As shown in Fig. 3(b), each cell enclosed by its polygonal faces contains one particle and its associated void, representing the overall dual-phase (solid-pore) structure of a granular medium. We use the open source library Voro++ [41] to tessellate the assembly obtained from DEM simulations. The Minkowski functionals and tensors are then used to study the morphology of the constructed cells [25,42]. For a specific cell K [see Fig. 3(c)], the associated Minkowski functionals W_0, W_1 and the Minkowski tensor $\mathbf{W}_1^{0,2}$ are defined as follows:

$$W_0(K) := \int_K dV, \tag{4}$$

$$W_1(K) := \frac{1}{3} \int_{\partial K} dA, \tag{5}$$

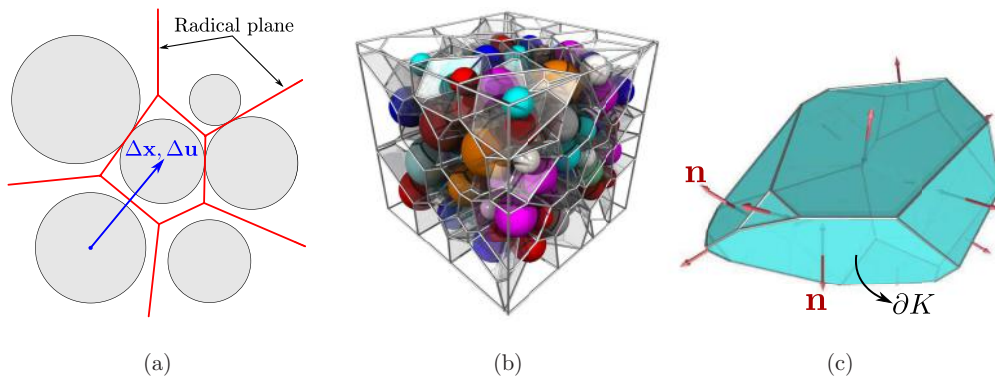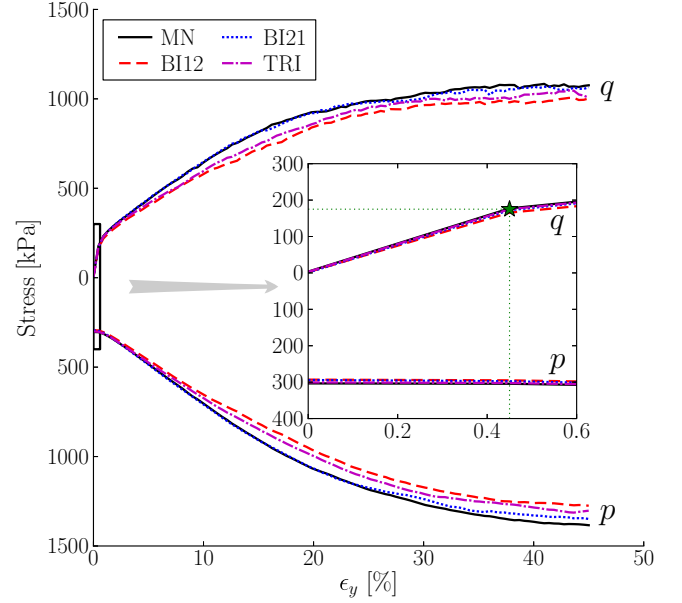$$\mathbf{W}_1^{0,2}(K) := \frac{1}{3} \int_{\partial K} \mathbf{n} \otimes \mathbf{n}\, dA, \tag{6}$$

FIG. 3. (Color online) Radical Voronoi tessellation in (a) two and (b) three dimensions. Radical planes are shown as red lines in (a) and transparent glasses in (b). $\Delta \mathbf{x}$ and $\Delta \mathbf{u}$ are the relative position and displacement between the two neighboring particles, respectively. (c) A Voronoi cell K with surface ∂K and outward normal $\mathbf{n}$.

where $\mathbf{n}$ is the outer normal of surface ∂K of the cell. W_0 simply leads to the volume of cell K, which in the sequel will be denoted by V_L with the subscript L representing a local measure. By normalization, a dimensionless tensor $\mathbf{W}_L := \mathbf{W}_1^{0,2}/W_1$ with a unity trace is more appropriate to characterize the local anisotropy.

With V_L and $\mathbf{W}_L$, both the isotropic and the anisotropic properties of the local structure can be quantified. The isotropic quantity examined here is the local density, or local volume fraction $\phi_L = V_p/V_L$, where V_p is the volume of the enclosed particle in the cell. To characterize the local anisotropy, we follow Refs. [25,42] by defining

$$\beta = \frac{\lambda_{\max}}{\lambda_{\min}} - 1, \tag{7}$$

where $\lambda_{\min}$ and $\lambda_{\max}$ are the minimum and maximum eigenvalues of $\mathbf{W}_L$, respectively, which are both positive since all Voronoi cells are convex with finite volumes. β measures the anisotropic intensity of a cell, and $\beta = 0$ corresponds to an isotropic cell. The anisotropic orientation can be quantified from the characteristic eigenvector $\boldsymbol{\nu}$ associated with $\lambda_{\max}$.

D. Local deformation

The local affine deformation field $\boldsymbol{\Gamma}$ for each particle relative to its nearest neighbors [see Fig. 3(a)] can be determined by minimizing the following D^2 [12,15,24]:

$$D^2 = \sum_{\text{neigh}} [\Delta \mathbf{x}' - (\boldsymbol{\delta} + \boldsymbol{\Gamma}) \cdot \Delta \mathbf{x}]^2, \tag{8}$$

where the summation is taken over the nearest neighbors of the reference particle, and $\Delta \mathbf{x}$ and $\Delta \mathbf{x}'$ are the relative position between the reference particle and its neighbor before and after the deformation, respectively. $\boldsymbol{\delta}$ is the Kronecker delta. $\boldsymbol{\Gamma}$ can be calculated according to

$$\boldsymbol{\Gamma} = \mathbf{X} \cdot \mathbf{Y}^{-1} - \boldsymbol{\delta}, \tag{9}$$

where

$$\mathbf{X} = \sum_{\text{neigh}} \Delta \mathbf{x}' \otimes \Delta \mathbf{x}, \quad \mathbf{Y} = \sum_{\text{neigh}} \Delta \mathbf{x} \otimes \Delta \mathbf{x}.$$

The local strain tensor is thus obtained from the symmetric part of $\boldsymbol{\Gamma}$: $\boldsymbol{\epsilon}_L = -(\boldsymbol{\Gamma} + \boldsymbol{\Gamma}^T)/2$, wherein the minus sign is present due to a compression positive convention adopted here. The volumetric strain ϵ_L^v and the deviatoric strain ϵ_L^q are determined such that they are work conjugate to the stresses defined in Eq. (3):

$$\epsilon_L^v = \operatorname{tr} \boldsymbol{\epsilon}_L, \tag{10a}$$

$$\epsilon_L^q = \sqrt{\frac{2}{3} \boldsymbol{\epsilon}_L^{\text{dev}} : \boldsymbol{\epsilon}_L^{\text{dev}}}, \tag{10b}$$

where $\boldsymbol{\epsilon}_L^{\text{dev}}$ ($= \operatorname{dev} \boldsymbol{\epsilon}_L$) is the deviatoric local strain tensor.

A granular material may also experience nonaffine deformation when subjected to external loading. The nonaffine deformation is attributable to many complex behaviors of granular media, such as plasticity [11,12,15] and strain localization [36]. For each particle, the nonaffine displacement is determined by subtracting the globally prescribed mean

displacements, i.e., the affine displacements [17,24]:

$$\tilde{\mathbf{u}} = \mathbf{u} + \Delta \boldsymbol{\epsilon} \cdot (\mathbf{x} - \mathbf{x}_{\text{rest}}), \tag{11}$$

where $\mathbf{u}$ is the displacement of the treated particle for the measured time interval, $\Delta \boldsymbol{\epsilon}$ is the global strain tensor, $\mathbf{x}$ is the particle position before the deformation, and $\mathbf{x}_{\text{rest}}$ is the position at rest (i.e., fixed in space) during the deformation.

III. RESULTS AND DISCUSSION

The local volume fluctuation serves as a good measure of Edwards' compactivity (or effective temperature) for granular media. The local strain and nonaffine displacement field can also provide useful information on the characterization of macroscopic properties such as plasticity. We will examine these features of the local quantities defined above in this section, with a focus on their fluctuations and spatial correlations. A shear-transformation-zone model will be further formulated and applied to the prediction of shear behavior of the granular assemblies as shown in Fig. 2.

A. Local structure

1. Volume fluctuations and compactivity

We first examine the radial distribution function (RDF) $g(\mathbf{r})$ of the four assemblies to investigate the influence of the applied shear. The property of RDF is believed to be distinct for a solidlike granular medium as compared to a fluidlike one. Figure 4 shows the RDFs at three different shearing levels. From the insets of the figure, we observe nearly isotropic RDFs on the three orthogonal planes for all four cases, which is consistent with that reported in Ref. [36] where the loading mode is simple shear. Nevertheless, it is seen that the pair correlation in the isotropic stress plane (x-z plane) is much weaker than those in the other two anisotropic stress planes (x-y and z-y). The isotropic property enables us to describe the RDF as a function of a single scalar variable r which measures the pair distance. Notably, the RDFs of all assemblies remain almost unchanged during the shearing course despite certain small fluctuations. In MN, the first peak is found to appear at a distance of one particle diameter; in BI12 and BI21, three local peaks are observed at distances corresponding to $\binom{3}{2} = 3$ combinations of the two types of particle diameter; in TRI, the RDF shows a similar shape to MN with the first local peak appearing at a distance of ensemble average diameter which is smoothed out from $\binom{4}{2} = 6$ local peaks. Figure 4 confirms that all the assemblies are solidlike [38–40].

Aste and co-workers [6,43] reported that the fluctuation of local volumes within a monodisperse granular assembly follows a shifted gamma distribution function (GDF):

$$P(V_L; s, \theta, l) = \frac{1}{\Gamma(s)\theta^s} (V_L - l)^{s-1} e^{-(V_L - l)/\theta}, \tag{12}$$

where s, θ, and l are the shape, scale, and location parameters, respectively. $\Gamma(\cdot)$ denotes the gamma function. To account for polydispersity, we normalize V_L with the enclosed particle volume, i.e., $V_L/V_p = \phi_L^{-1}$, which is the inverse local volume fraction, and propose the following mixed-GDF:

$$P_{\text{mix}} = \sum_i \alpha_i P_i, \tag{13}$$

(a) MN
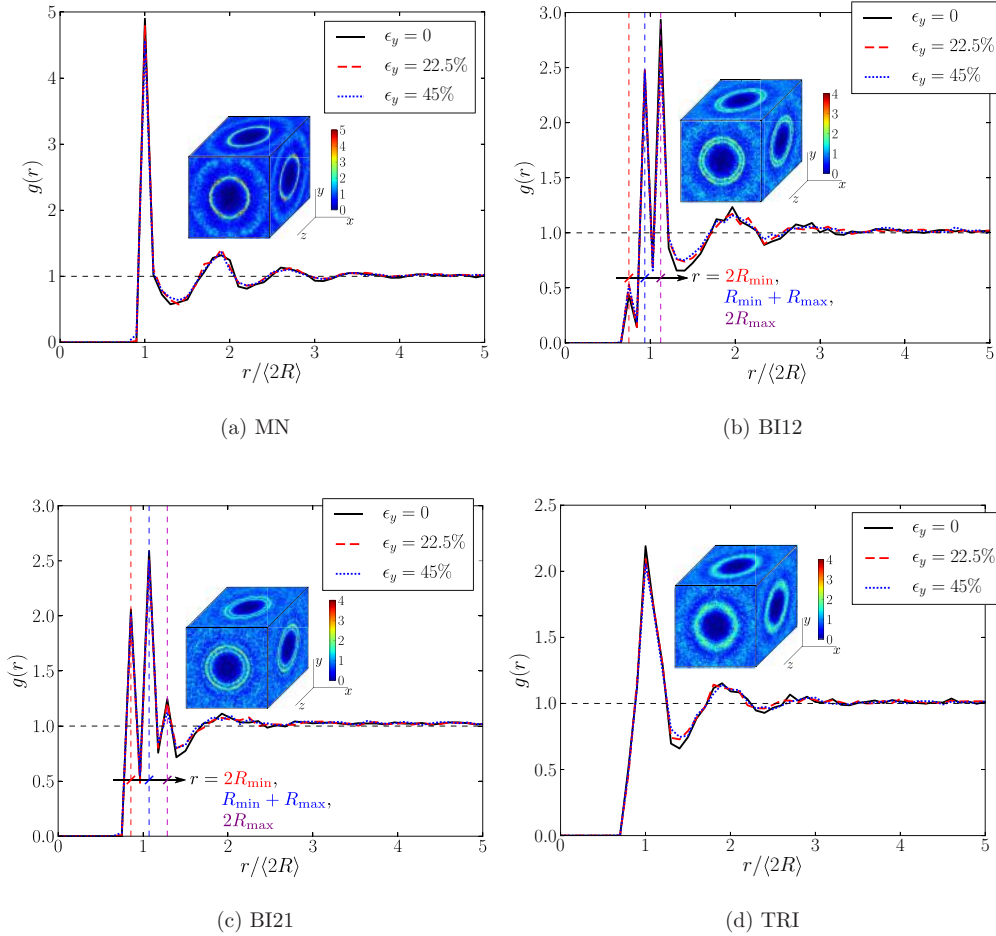

(b) BI12

(c) BI21

(d) TRI

FIG. 4. (Color online) Radial distribution function for the four assemblies at three different shearing levels. The measured radial distance interval is 0.1 mean particle diameter. The insets show the color map resolving of $g(\mathbf{r})$ onto three orthogonal planes at $\epsilon_y = 45\%$. The presented distance range in the insets is $x,y,z/\langle 2R \rangle = \pm 2$.

where P_i is the contributed probability of the ith group of particles (grouped by particle radius). α_i is the weight factor of the group which is set equal to the proportion of particle number.

As expected, the local volumes in the monodisperse assembly MN yields the gamma distribution, as shown in Fig. 5(a). The distribution changes slightly with the shearing process, i.e., the variation of fluctuations slightly increases while the peak drops with the applied shear. However, after normalization with the mean value, the distributions of $\phi_L^{-1}/\langle \phi_L^{-1} \rangle$ $(= V_L/\langle V_L \rangle)$ at different shearing levels collapse to one single GDF curve [see inset of Fig. 5(a)]. In the two bidisperse cases, two peaks for $P(\phi_L^{-1})$ corresponding respectively to the small (S) and large (L) particle groups are observed. In both cases, the first higher peak is contributed by the large particles, while the second lower one is contributed by the small particles (see dotted curves). This is not surprising since large particles generally have larger volume fractions (smaller ϕ_L^{-1}) than small particles in a typical mixture. Due to less small particles in BI12, the second peak in BI12 is much less distinct than that in BI21. Again, the distributions in both assemblies at different shearing levels are rather close. The local volume distributions for large particle group (L) and small particle group (S) are separately plotted in the insets

of Figs. 5(b) and 5(c). After normalization with the mean value, the data points for each group at different shearing levels collapse to their respective GDF curves. In either BI12 or BI21, the distribution of the large particle group has a higher peak value and smaller variation than that of the small particle group, and this trend does not change with the relative proportion of the two particle groups. The observations in the tridisperse assembly are similar to those in the bidisperse assemblies. Nevertheless, the local peaks in the tridisperse case appear to be totally smoothed out, which results in a single global peak.

As V_L is a measure of the local free volume (accessible volume for a particle), its distribution serves as a good indicator for Edwards' compactivity χ through [6,7]

$$\chi = \frac{\sigma_{V_L}^2}{\langle V_L \rangle - (V_L)_{\min}}, \qquad (14)$$

where σ_{V_L} denotes the standard deviation of V_L. Figure 5 shows almost identical distribution for the normalized local volumes at different shearing levels, which indicates the compactivity of each assembly remains constant during the shearing. By shifting and scaling the data, Aste and co-workers [6,43] found the local volume fluctuation follows a k-gamma distribution, where the parameter k can be linked with the number of
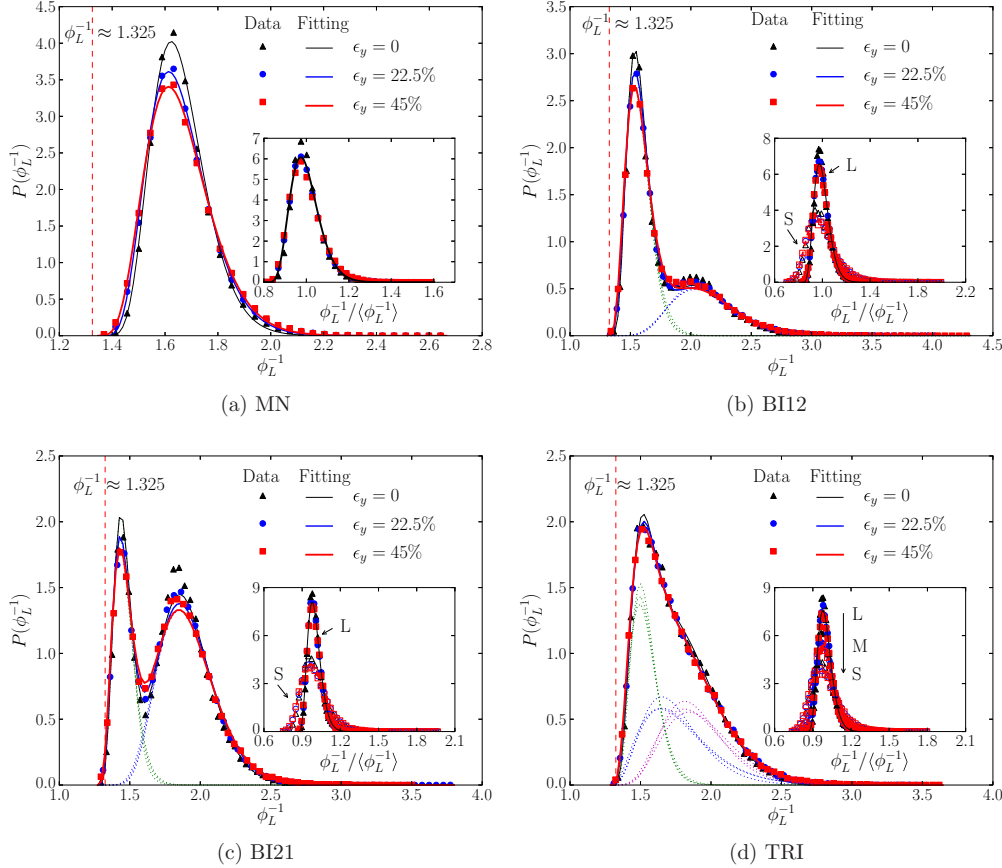
FIG. 5. (Color online) Local density distribution for the four assemblies at different shearing levels. GDF is used to fit the data in MN; while in polydisperse assemblies, a mixed-GDF is used [44]. The dotted curves show the contributions from individual groups. In the insets, the quantity is normalized by its mean value. And the distributions for different groups are distinguished. $\phi_L^{-1} \approx 1.325$ corresponds to the theoretical largest volume fraction achievable in a random monodisperse assembly [43].

elementary cells that exchange volumes (energy) with each other when subjected to external loading, and can be calculated from

$$k = \frac{\left[\langle\phi_L^{-1}\rangle - (\phi_L^{-1})_{\min}\right]^2}{\sigma_{\phi_L^{-1}}^2} = \frac{\langle V_L\rangle - (V_L)_{\min}}{\chi}. \qquad (15)$$

We plot the data of different particle groups (eight groups from the four assemblies) at three shearing levels in Fig. 6(a), and find that they all roughly collapse to the same k-gamma distribution with $k \in [5,7]$. In Fig. 6(b) we further plot the evolution of χ in all eight groups. Clearly, the compactivity for each of the groups remains roughly constant during the entire shearing process. This is not surprising since we have imposed the constraint of constant volume on the assemblies. However, within the same polydisperse assembly, the compactivities for different groups differs from one another. Since the zeroth law of thermodynamics requires a single temperature for an equilibrated mixture, this indeed suggests that the effective temperatures over different particle groups in a slowly sheared system are nonequilibrated, and the compactivity in the small particle group is slightly smaller. In addition, we observe a smaller difference among groups in tridisperse assembly than that in bidisperse ones, which indicates the compactivity is more equilibrated when the packing is better

graded. Pertaining to the equilibrium of compactivity among different subsystems, we notice that Refs. [22,45] reported a same effective temperature between small particle and large particle groups by calculating the ratio of diffusivity and mobility following a similar definition of temperature to that of conventional fluids, while a more recent study [8] also showed the failure of the zeroth law on compactivity between a bath and a subsystem of granular disks. A possible attributable reason for the observed difference is that in Refs. [22,45], the particle rearrangements are more prevalent and the system is more fluidlike such that the subsystems (groups) can possibly reach equilibrium easily, while the granular systems treated in the current study and in Ref. [8] are of high density and subjected to mild agitation.

2. Fluctuations of anisotropy

The local Voronoi cell and volume fraction help to measure the isotropic character of the local structure of granular media. A disordered granular material, however, is inherently anisotropic even if isotropic particles (i.e., spheres) are used [25]. Anisotropy underpins the key mechanical and physical properties of granular media (e.g., permeability and thermal conductivity), and the related research has drawn much attention [26,33,46,47]. It is interesting to examine the feature
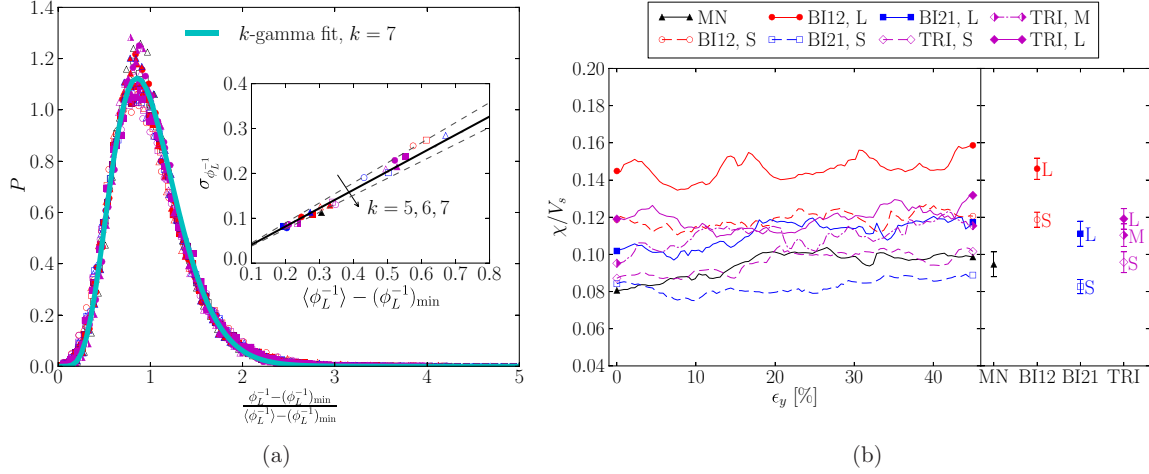
FIG. 6. (Color online) (a) k-gamma fitting of normalized local density. The collapsed symbols include data from all the eight groups in the four assemblies and at three different shearing levels ($\epsilon_y = 0, 22.5\%$, and 45%). (b) Evolution of χ measured in the four assemblies for different groups, and the mean and standard deviation (shown as error bar) of χ throughout the shearing process. χ is in the unit of volume and is normalized by the volume of the smallest particle $V_s \approx 0.0335$ mm^3.

of local anisotropy in the granular media here. We plot the normalized local anisotropic intensity $\hat{\beta} = \beta/\langle\beta\rangle$ in Fig. 7. It is interesting to observe that the distribution of the local anisotropic intensity also follows a mixed-gamma distribution. The distribution in each assembly remains almost unchanged during the shearing process. The polydisperse cases only give rise to a global peak without any local peaks where $\hat{\beta}$ is slightly smaller than 1. The vanishing probability at $\hat{\beta} = 0$ indicates there is almost no isotropic cell existing in the assembly regardless of the applied stress state being isotropic or anisotropic. The observation holds even in the monodisperse assembly. The insets show the anisotropic intensity in each particle group (S, M, or L) which can be described by an individual GDF. Generally, the small particle group is more anisotropic than the large particle group, due to lower volume fraction (see the correlation of volume fraction and anisotropy in Sec. III C 1).

In addition to the anisotropic intensity, we define the following tensor for an assembly to account for the anisotropic orientation in a similar form to the contact-normal-based fabric tensor [48]:

$$\mathbf{F} = \int_\Theta E(\Theta)\, \boldsymbol{\nu} \otimes \boldsymbol{\nu}\, d\Theta = \underbrace{\frac{1}{N_p} \sum_{N_p} \boldsymbol{\nu} \otimes \boldsymbol{\nu}}_{\text{Discrete form}}, \qquad (16)$$

where $\boldsymbol{\nu}$ is the anisotropic orientation of the local Voronoi cell (eigenvector associated with the maximum eigenvalue of $\mathbf{W}_L$), and N_p is the total particle number which is equal to the total Voronoi cell number. $E(\Theta)$ characterizes the probability density of the spatial distribution, which can be visualized by means of a three-dimensional rose diagram as shown in Fig. 8 for the TRI case. Its approximation by a second-order Fourier expansion is also shown in the figure. Interestingly, although the anisotropic intensity distribution cannot differentiate an isotropic stress state ($\epsilon_y = 0$) from an anisotropically sheared state, the anisotropic orientation differs in the two cases distinguishably. In an isotropic stress state, the

anisotropic local cells are randomly orientated which results in a globally isotropic structure for the entire assembly [i.e., $E(\Theta)$ resembles a sphere]. When the assembly is subjected to anisotropic shearing, the local cells gradually adjust internally towards a more effective global structure to accommodate the external loading with preferable orientation along the deviatoric shear loading direction [now $E(\Theta)$ resembles an ellipsoid with its long axis aligning with the shear direction]. These characters of $\mathbf{F}$ bear great similarities to those of a contact-normal or particle-orientation-based fabric tensor (see Fig. 5 in Ref. [47]), which has been repeatedly explored recently in *soil mechanics* [33,34]. Hence the newly defined tensor in Eq. (16) seems to be an alternative for the *fabric tensor*, but it incorporates more morphological information than the old ones and helps to unify the characterization of structural isotropy and anisotropy through one tessellation. In addition, this new tensor offers proper definition of local anisotropy and is thus applicable to the study of anisotropy fluctuations, which is an important feature lacked by otherwise defined forms.

B. Local deformation

1. Shear strain

We measure the instant local deviatoric strain within a global deformation interval of $\Delta\epsilon_y = 0.9\%$ at three reference stages. We take the case of TRI as an illustrative example and show its results in Fig. 9. The distribution probability of ϵ_L^q in TRI at the initial stage of shearing ($\epsilon_y = 0$) shows a peak with a magnitude ($\sim 1\%$) close to the global shearing strain, and the variation in the distribution is narrow. Its maximum value ($\sim 10\%$) at the initial stage is much smaller as well compared to those in the later shearing stages. These observations indicate that the overall deformation of the sample is relatively homogeneous, and the assembly undergoes almost pure elastic deformation at this early stage as the color map displays dominant blue and cyan; while at the two later shearing states, the deformation field becomes highly
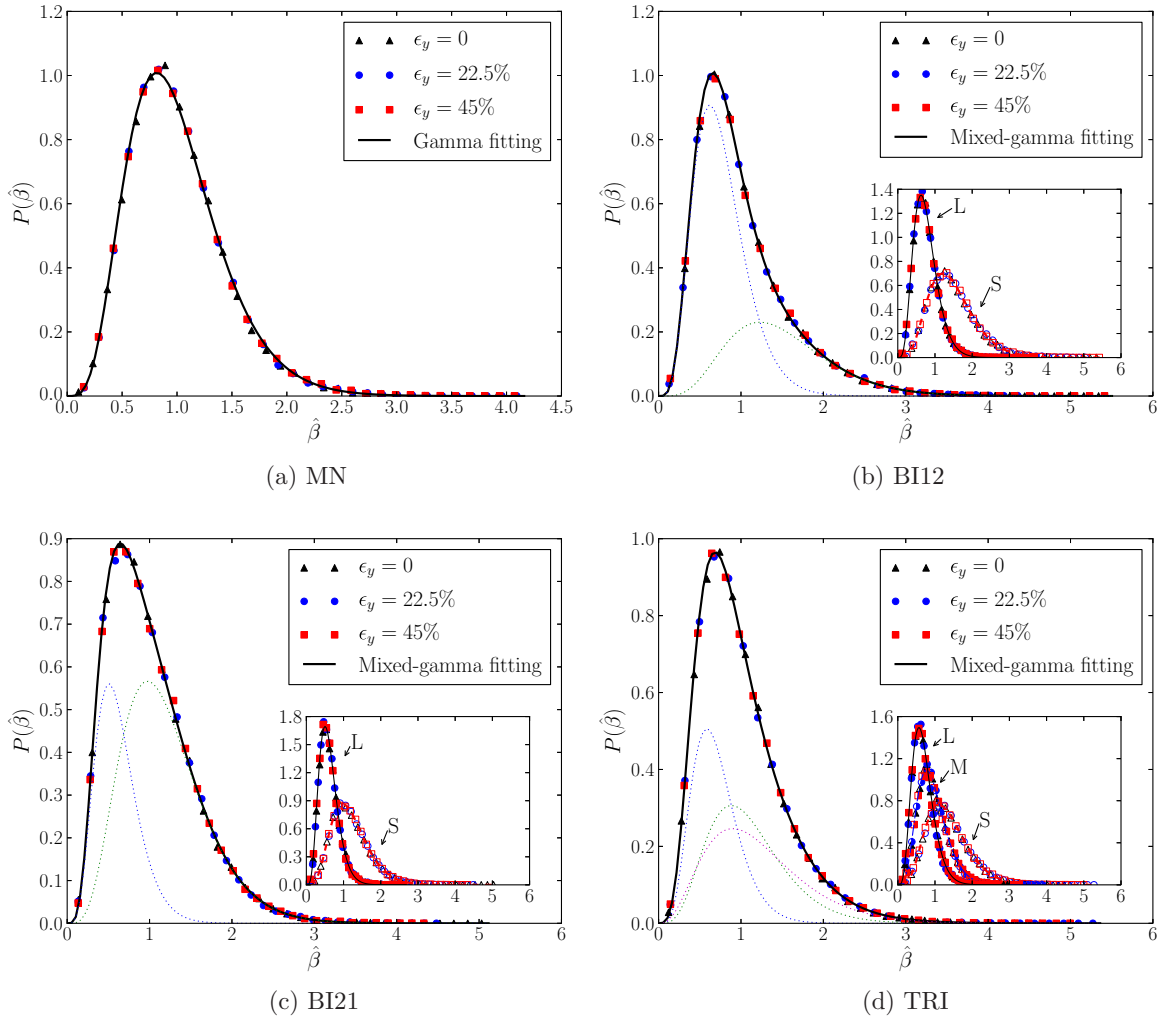
FIG. 7. (Color online) Probability distribution of the local anisotropic intensities for the four assemblies at different shearing levels. GDF is used to fit the data in MN, while mixed-GDF is used for the other cases. The insets distinguish the distributions for different groups.

inhomogeneous with significantly concentrated shearing zones wherein the maximum ϵ_L^q exceeds 30%. These intensively
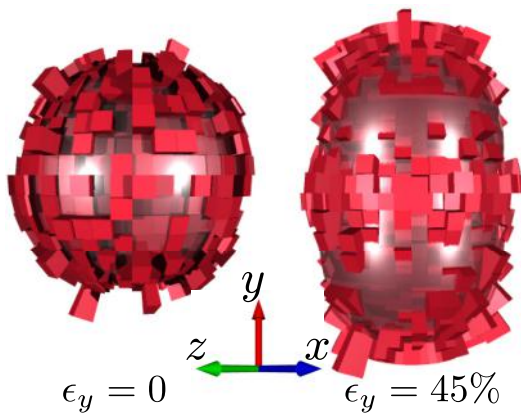

FIG. 8. (Color online) Rose diagram of the spatial distribution of the local anisotropic orientations in TRI at the initial stress isotropic state ($\epsilon_y = 0$) and the sheared steady state ($\epsilon_y = 45\%$). The overlaid transparent membranes are the corresponding Fourier approximations.

sheared zones can be identified as STZs within small clusters of particles which are considered to be the fundamental units of plasticity in a sheared amorphous material [10]. These STZs are "plasticity carriers" which makes them comparable to dislocations in crystals. However, since they are varying in space at different shearing levels, STZs formed at an early stage may be annihilated in a location of the assembly and new STZs may develop elsewhere at a later stage, which is evident from Fig. 9. The observation is indeed consistent with the STZ theory that once a STZ transforms it cannot repeatedly undergo the same transformation unless subjected to a reverse shearing [15]. Also the STZs shown in Fig. 9 are more prevalent at $\epsilon_y = 45\%$ and the shearing intensities are larger than those at $\epsilon_y = 22.5\%$. Moreover, at all three shearing stages, we observe a power-law decay at the tail part of the distribution curves for the local shear strains. This fact implies a high correlation for these local STZs which will be examined later. The power-law decaying distribution can also be observed in the cooperative motion of dislocations in crystal plasticity [49,50]. Due to the constant volume constraint assumed in the study, the result of volumetric strain (dilation) is not presented. We nevertheless notice in our study that ϵ_L^v
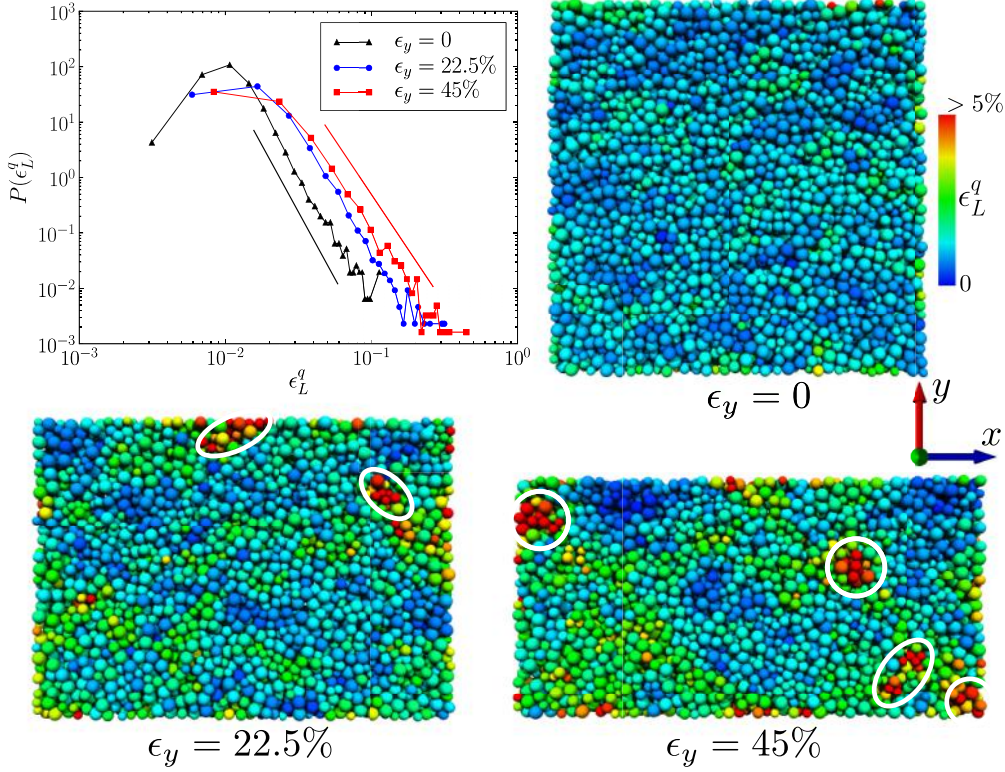
FIG. 9. (Color online) Distribution of local deviatoric strain ϵ_L^q in TRI within the applied deformation interval $\Delta\epsilon_y = 0.9\%$. $\epsilon_y = 0, 22.5\%$, and 45% are three reference states. The color maps show the x-y plane resolving of ϵ_L^q for a slice with a thickness of four mean particle diameter. Circled regions are identified as STZs.

and ϵ_L^q are weakly correlated with the Pearson correlation coefficient ~ 0.1 at the shearing state of all four assemblies.

To measure the spatial correlation of the local shear strain, we define the following normalized function:

$$C_\epsilon(\mathbf{r}) = \frac{\langle\epsilon(\mathbf{r})\epsilon(\mathbf{0})\rangle - \langle\epsilon(\mathbf{0})\rangle^2}{\langle\epsilon(\mathbf{0})^2\rangle - \langle\epsilon(\mathbf{0})\rangle^2}, \qquad (17)$$

where ϵ measures the deviation between the two components of the local strain tensor in the global principal directions, e.g., on the x-y plane, $\epsilon := (\epsilon_L)_{yy} - (\epsilon_L)_{xx}$. In doing so, ϵ is comparable to $(\epsilon_L)_{xy}$ used in a simple shear test [23]. Alternatively, the local deviatoric tensor may be used directly (i.e., $\epsilon = \boldsymbol{\epsilon}_L^{\text{dev}}$). Then the multiplication should be replaced with the tensorial double contraction accordingly. The second way (using tensor measure) will yield a similar spatial correlation pattern shown in Fig. 10 with a relative smaller C_ϵ as compared to the former one (using scalar measure), but will lead to complicated calculations. We hereby adopt the scalar measure here.

Shown in Fig. 10, the local shear strains have a long-range spatial correlation with a correlated distance greater than 10 mean particle diameter.[1] In all the three planes, we observe a fourfold pattern with negative correlations in the principal stress directions and positive correlations in the diagonal shear

directions, which is consistent with that reported in Ref. [23] (their principal directions are in diagonal for the simple shear test mode and their study was performed on colloidal glass). However, there are also notable differences for the three planes. In both x-y and z-y cross sections which are the two stress deviatoric planes, the correlations are apparently strong and long ranged. A symmetric pattern in the z-y plane is observed, indicating the shear deformations occur uniformly in both diagonal directions. Comparatively, the deformation in the x-y plane is more prevalent in one diagonal direction over the other. By comparing our results with those reported in Ref. [23] [Fig. 2(e) therein], the correlation patterns in these two planes (x-y and z-y) confirm that our simulation is within the shearing dominated regime as mentioned in Sec. II A. However, the correlation pattern in the x-z cross section (the stress isotropic plane) indicates a thermal-effect dominated test (where the modified Péclet number Pe* < 1) as shown in Ref. [23] [Fig. 1(d) therein], and the correlations are much weaker and shorter ranged than those in the other two planes. The observed fourfold pattern in the x-z plane can be regarded as the elastic response of the material to the existence of STZs, as the pattern is reminiscent of the Eshelby solution of strain field around a circular inclusion [23,51,52] and the STZs play a similar role of the inclusions.

2. Nonaffine displacement

The nonaffine displacement fields in TRI are shown in Fig. 11. Notably, the probability distributions of $|\tilde{\mathbf{u}}|$ in TRI at the three different reference stages are very similar to those

---

[1]We cut this distance for evaluation due to the limitation in sample size. At the steady state of shear, the shortest dimension (in the y axis) of the assembly is roughly 20 mean particle diameter.
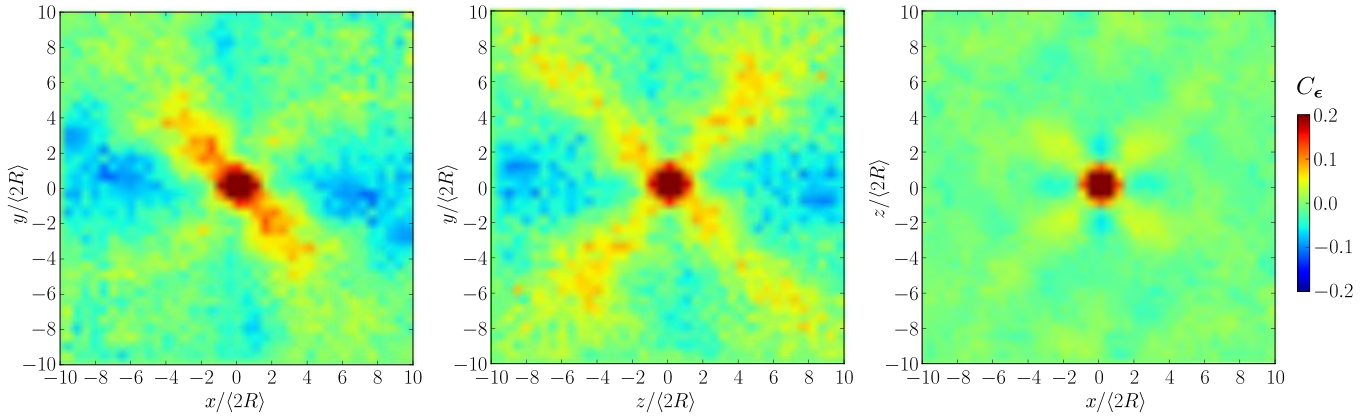
FIG. 10. (Color online) Spatial correlation of local shear strains at steady state in BI21 resolved onto three orthogonal cross sections. The global strain interval is 0.9%. The cross-sectional slices are reconstructed with a thickness of three mean particle diameter. The measured distance interval is 0.5 mean particle diameter.

of ϵ_L^q. At the initial stage ($\epsilon_y = 0$), the assembly undergoes almost pure elastic deformation, thus there are very few particles having nonaffine displacements with rather small magnitude. The vast majority of the particles have no nonaffine displacements at all (dark blue in the color map), and the maximum value is less than 0.08 mm. With the increase of shearing levels, there are increasing numbers of particles experiencing large nonaffine displacements. At the steady state ($\epsilon_y = 45\%$), the maximum $|\tilde{\mathbf{u}}|$ even exceeds the medium-sized particle radius, i.e., greater than 0.25 mm. A similar power-

law decay is also observed in the figure for the probability distribution of nonaffine displacements. By comparing Fig. 11 with Fig. 9, we notice that the spots subjected to large nonaffine displacements are largely coincident with the STZs, though the former are not as clustered as the STZs. This indicates that both quantities may be considered as good measures of local plasticity (see the Pearson correlation of the two quantities in Sec. III C 1).

Although the absolute magnitudes of the nonaffine displacements increase with the applied shearing, the normalized
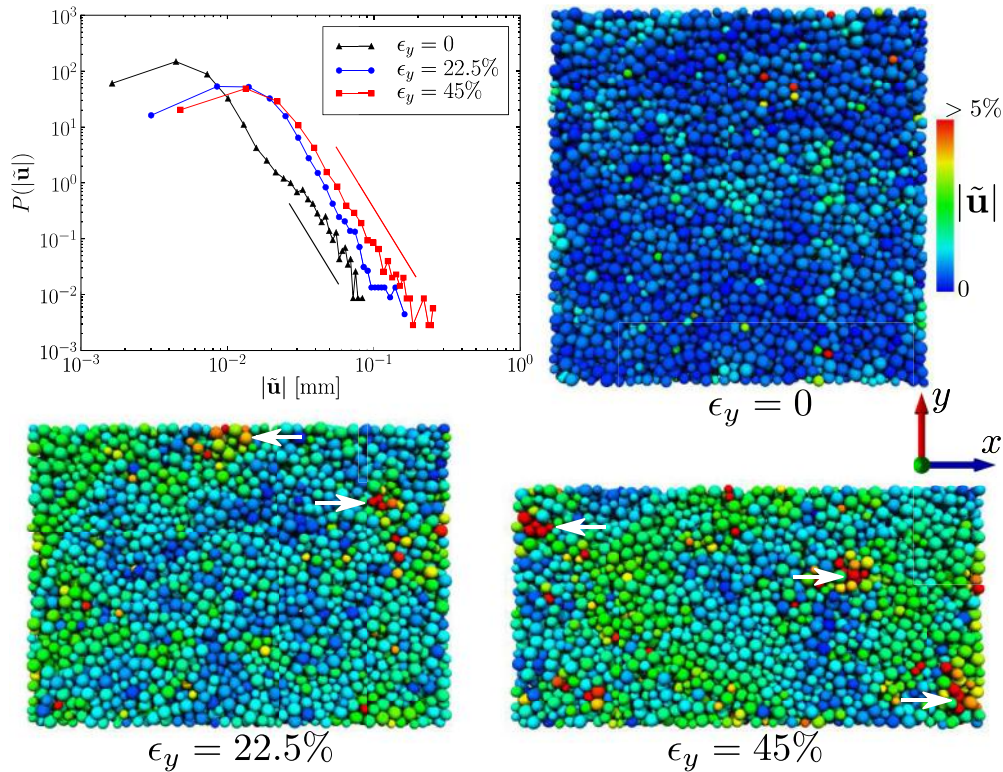

FIG. 11. (Color online) Distribution of local nonaffine displacement $|\tilde{\mathbf{u}}|$ in TRI at different reference states within a same global deformation interval $\Delta\epsilon_y = 0.9\%$. The color maps show the x-y plane resolving of $|\tilde{\mathbf{u}}|$. The slice is the same as that in Fig. 9. Spots undergoing large nonaffine displacements are highlighted with arrows.
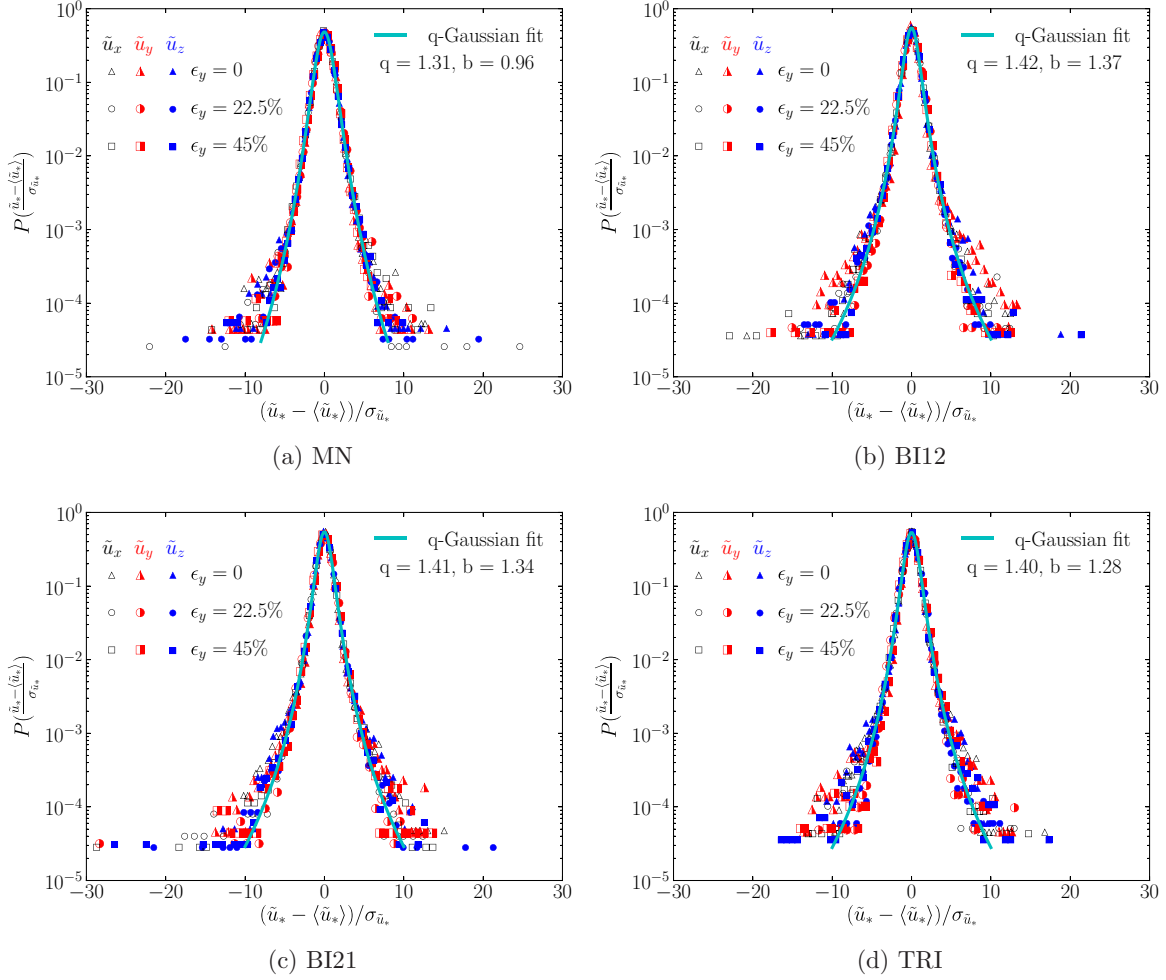
(a) MN

(b) BI12

(c) BI21

(d) TRI

FIG. 12. (Color online) Probability distribution of the nonaffine displacements for the four assemblies in the x, y, and z directions and at different shearing levels. The q-Gaussian distribution is used to fit the data with the probability density function $\propto [1 - b(1-q)(\frac{\tilde{u}_* - \langle \tilde{u}_* \rangle}{\sigma_{\tilde{u}_*}})^2]^{1/(1-q)}$. The fitted values of the two parameters q and b are given in the figure.

quantity $(\tilde{\mathbf{u}} - \langle \tilde{\mathbf{u}} \rangle)/\sigma_{\tilde{\mathbf{u}}}$ is found to follow the same distribution (well fitted by a q-Gaussian distribution) at the three different shearing levels as shown in Fig. 12. In the figure, the components of the nonaffine displacements in different directions ($\tilde{u}_x$, $\tilde{u}_y$, and $\tilde{u}_z$) are distinguished. The fluctuations of the nonaffine displacements stay isotropic (same distribution in all three directions) irrespective of the applied loading being isotropic or anisotropic. As the fluctuation is a measure of granular temperature, this observation confirms two key points: First, the applied shear plays a similar role to thermal activation for the granular assembly to relax which lends support to the statistical approach in describing the granular material behaviors; second, under the constraint of constant volume shearing, the granular temperature is maintained constant, which is consistent with our previous conclusion from examining fluctuations of the local volumes. Note that the granular media in their fluid-state counterparts may have anisotropic kinetic temperature [53].

The existence of a q-Gaussian distribution for the nonaffine displacements implies that the variables are long-range correlated [54,55], and it is also consistent with the observations of power-law decayed distributions in Figs. 9 and 11. It

is hence interesting to measure the spatial correlation of the nonaffine displacements $C_{\tilde{\mathbf{u}}}$ which is defined similar to Eq. (17):

$$C_{\tilde{\mathbf{u}}}(\mathbf{r}) = \frac{\langle \tilde{\mathbf{u}}(\mathbf{r}) \cdot \tilde{\mathbf{u}}(\mathbf{0}) \rangle - \langle \tilde{\mathbf{u}}(\mathbf{0}) \rangle^2}{\langle \tilde{\mathbf{u}}(\mathbf{0})^2 \rangle - \langle \tilde{\mathbf{u}}(\mathbf{0}) \rangle^2}. \qquad (18)$$

Note a vector measure is used here, e.g., on the x-y plane, $\tilde{\mathbf{u}} := (\tilde{u}_x, \tilde{u}_y)$. From the results shown in Fig. 13, we see that the correlation of nonaffine displacement displays relatively isotropic patterns in all three orthogonal planes, which differs essentially from that of the local shear strain. The correlation intensity is also higher for the nonaffine displacement (note that color bars in Figs. 10 and 13 have different ranges). The observation is consistent with that mentioned in Ref. [23]. The correlation is stronger in the two stress deviatoric planes (x-y and z-y) than that in the stress isotropic plane (x-z). This isotropic property of spatial correlation is in accordance with the observation of a vortexlike pattern of nonaffine displacements formed in the sheared granular media, and is favored by the proposition of an isotropic granular temperature as has been discussed before. The above observations on the
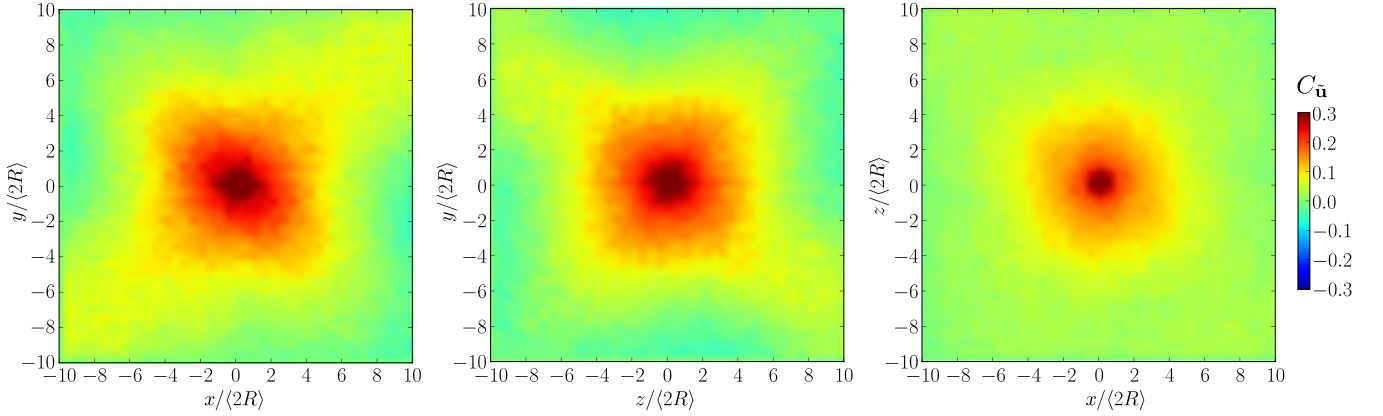
FIG. 13. (Color online) Spatial correlation of nonaffine displacements at steady state in BI21 resolved onto three orthogonal cross sections. The measurement is the same as that described in Fig. 10.

spatial correlations of shear strain and nonaffine displacement provide convincing evidence that there exists a long-range correlation on the deformation in slowly sheared granular media.

C. Further discussion

1. Cross correlation among local quantities

As already seen from Figs. 9 and 11, there exists a striking correlation between the local shear strains and the nonaffine displacements. It is further interesting to see how all local measurements are correlated with one another. Here we use the Pearson correlation coefficient calculated by

$$\rho_{\text{corr}}(X,Y) = \frac{\text{cov}(X,Y)}{\sigma_X \sigma_Y}, \qquad (19)$$

where X and Y are the chosen pairs from the four local measurements, i.e., local inverse density (ϕ_L^{-1}), local anisotropy (β), local shear strain (ϵ_L^q), and nonaffine displacement ($|\tilde{\mathbf{u}}|$); cov takes the covariance of the two quantities. The results are shown in Fig. 14. The most significant correlation is found between the local density and the local anisotropy. When the local structure tends to be looser (larger ϕ_L^{-1}), it becomes more anisotropic, which is reasonable since a denser structure is subjected to more constraints from the neighborhood and is hence more likely to possess a regular latticelike shape (and less anisotropic). This also explains why the small particle group is generally more anisotropic than the large particle group in polydisperse assemblies as observed in Fig. 7. The second most obvious correlation is between the local shear strain and the nonaffine displacement as previously mentioned
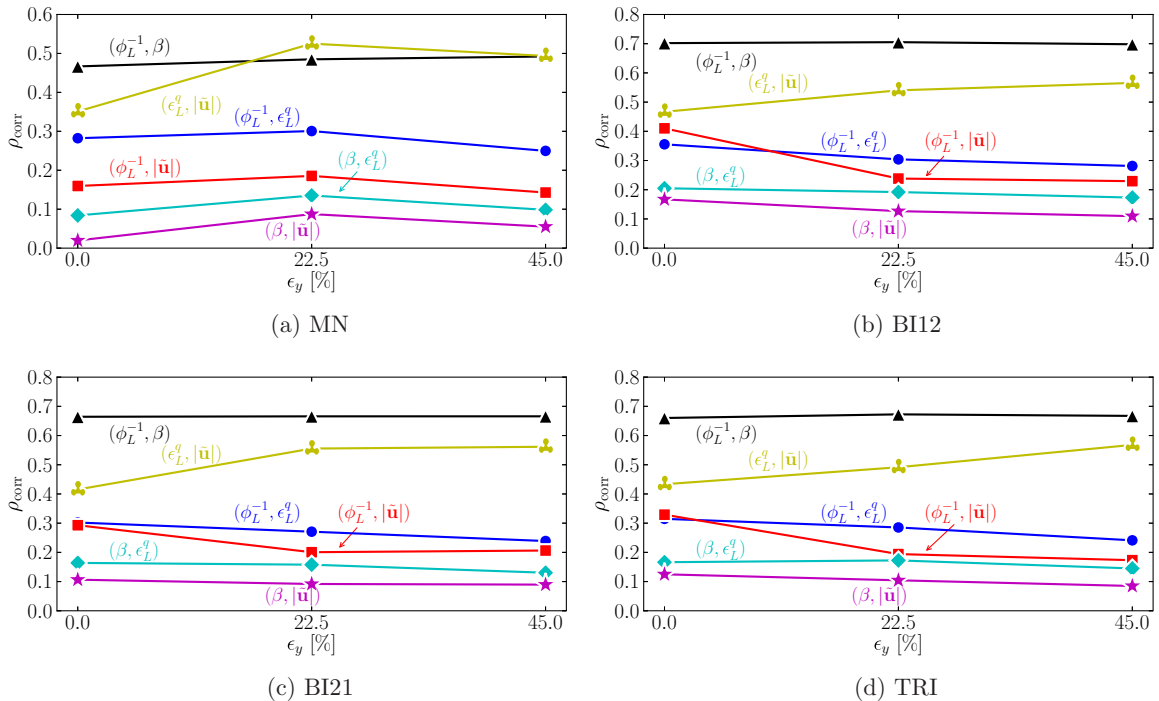

FIG. 14. (Color online) Pearson correlation among different local measurements in the four assemblies.

where the correlation coefficient is around 0.5. The third and fourth largest correlations are found between the local density with the two deformation quantities, which suggest that looser local units are more prone to generate plasticity, which is also consistent with our conceptual understanding that STZs are easier to become nucleated in regions that have larger free volumes. However, larger pressure levels may somehow reduce the effect of free volume [9] and result in a relatively small correlation coefficient (less than 0.3). Finally, the local anisotropy seems to be less important in determining the deformation, which is probably due to the use of spherical particles only in our simulations.

2. A pressure-dependent shear-transformation-zone model and its prediction

Various models have been available to describe the granular flow from the fluid to the solid regimes. For instance, the model developed by Jop *et al.* [32,56] can successfully predict the velocity profile for an intermediate dense granular flow (in, e.g., [57–59]) where the shear stress is dependent on the normal stress and the shearing rate. When approaching the quasistatic limit (e.g., the shear rate becomes zero), their formulation recovers the classic Drucker-Prager elastoplasticity model which has been discussed extensively in the modeling of geomaterials and will not be entailed here. Of particular interest here is the modification of the STZ model to the prediction of the material behavior as presented in Fig. 2, as an alternative correlation to the previous local analyses. In its original formulation, the STZ model assumes the material is pressure insensitive or is subjected to constant-pressure shearing as demonstrated by Ref. [14] based on Demkowicz and Argon's data [38–40]. The STZ model in the simplified form can be written

$$\frac{d\tilde{q}}{d\epsilon_y} = \tilde{G}\left(1 - \frac{2\zeta_0}{Q_0}e^{-1/\tilde{\chi}}Q(\tilde{q})\right), \tag{20a}$$

$$\frac{d\tilde{\chi}}{d\epsilon_y} = \frac{2\zeta_0}{c_0 Q_0}e^{-1/\tilde{\chi}}\tilde{q}Q(\tilde{q})(\tilde{\chi}_\infty - \tilde{\chi}), \tag{20b}$$

where

$$Q(\tilde{q}) = R(\tilde{q})[1 - m_0(\tilde{q})],$$

$$R(\tilde{q}) = \int_0^{\tilde{q}}(\tilde{q} - \tau)\tau\, e^{-\tau}\, d\tau,$$

$$m_0(\tilde{q}) = \begin{cases} 1 & \text{if } \tilde{q} \leqslant 1 \\ 1/\tilde{q} & \text{otherwise.} \end{cases}$$

The symbols and their physical meanings are briefly summarized as follows. $\tilde{q}$ and $\tilde{G}$ are the normalized deviatoric stress and the elastic modulus (initial slope of the q-ϵ_y curve) in the

unit of initial yield stress q_y (i.e., $\tilde{q} = q/q_y$ and $\tilde{G} = G/q_y$). Q_0 is a model parameter characterizing the interplay between the shearing rate and the STZ transition time, and can be calculated from $Q_0 = 2\zeta_0 e^{-1/\tilde{\chi}_\infty}Q(\tilde{q}_\infty)$ to ensure the availability of steady state. Here $\tilde{\chi}$ is the dimensionless effective temperature which is a normalization with respect to the characteristic STZ formation energy. $\tilde{\chi}_\infty$ and $\tilde{q}_\infty$ are the quantities at the final steady state. ζ_0 and c_0 are two constants reflecting the typical particle number in a STZ and the configurational specific heat per particle, respectively. The function $m_0(\tilde{q})$ quantifies the STZ orientational bias: Before yielding ($\tilde{q} \leqslant 1$), there is no bias thus $m_0 = 1$; while at larger deviatoric stress, m_0 is much smaller than 1. Function $R(\tilde{q})$ describes the STZ transition rate which depends on the magnitude of deviatoric stress (Ref. [60] included a free-volume factor into the formulation to account for dilatancy effect which is neglected here due to the imposed volume constraint). $Q(\tilde{q})$ guarantees no STZ transition within an elastic region. Note that we omit two extra equations in the complete STZ formulation governing the evolution of STZ density and orientational bias and choose to use the simplified form above.

As previously discussed, our systems maintain nearly constant effective temperatures under constant volume shearing. All four assemblies show an evident pressure-sensitive feature with continuous increase of deviatoric stress and pressure level (see Fig. 2). Since the STZ formation energy is also pressure dependent (it will be harder to activate a STZ transition under larger confining pressure), the normalized effective temperature $\tilde{\chi}$ will still evolve in our cases. Thus Eq. (20) is also deemed as applicable here and $\tilde{\chi}$ will decrease with the increase of p due to the requirement of larger STZ formation energy. The evolution of mean stress can be formulated similarly to the evolution of density in constant-pressure shearing as given in Ref. [14]:

$$\frac{dp}{d\epsilon_y} = \frac{2\zeta_0}{c_1 Q_0}e^{-1/\tilde{\chi}}\tilde{q}Q(\tilde{q})[p_\infty e^{-(\tilde{\chi}-\tilde{\chi}_\infty)} - p], \tag{21}$$

where c_1 is an additional parameter similar to c_0. The calibrated parameters are summarized in Table II. Note that some of the parameters can be determined directly from the simulation curves in Fig. 2, but others like dimensionless effective temperature $\tilde{\chi}$, c_0, and c_1 are more or less phenomenological and their values are chosen similar to those used in Ref. [14]. The model prediction is shown in Fig. 15 in comparison with our simulation data on the four assemblies. Evidently, the modified STZ model captures the material behavior reasonably well. The pressure dependency of granular media during the shear process can be well reproduced by the model. While the performance of the STZ model can be further improved, its

TABLE II. Parameters used in the STZ model for the four assemblies.

q_y (kPa)	q_∞ (kPa)	p_∞ (kPa)	$\tilde{G}$	ζ_0	$\tilde{\chi}_0$[a]	$\tilde{\chi}_\infty$	c_0	c_1
165–177	970–1050	1275–1384	1/0.0045[b]	10	0.08	0.065	0.16	0.45

[a]The dimensionless effective temperature prior to shear. $\tilde{\chi}_0 = 0.08$, $\tilde{q}_0 = 0$, and $p_0 = 300$ kPa form the initial value problem of Eqs. (20) and (21).

[b]0.45% is the identified strain at initial yield point (marked by a star in the inset of Fig. 2).
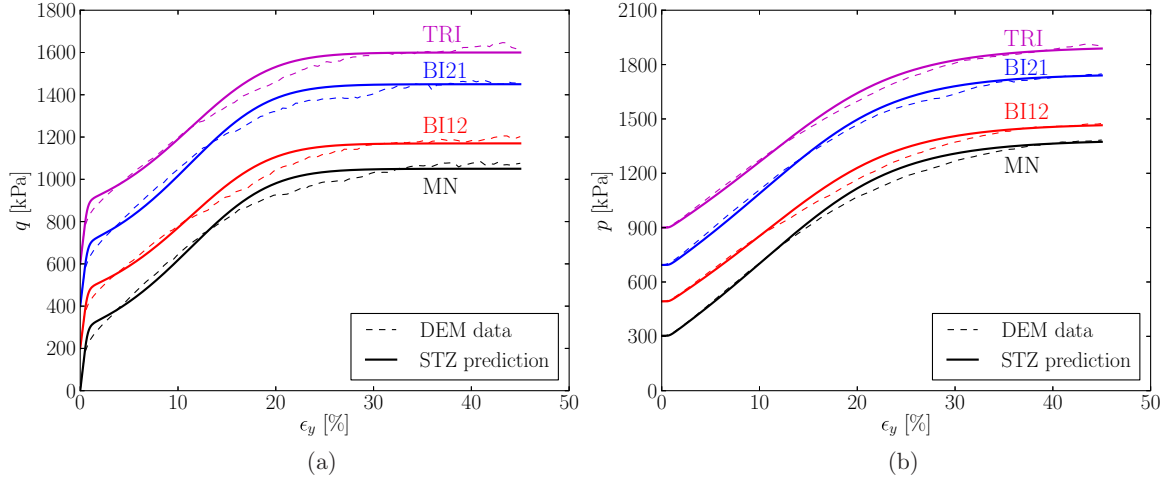
FIG. 15. (Color online) Comparison of the STZ model predictions of (a) deviatoric stress and (b) mean stress against the DEM data. The curves for the different cases are shifted upwards with an interval of 200 kPa for clarity of presentation.

study is not the focus of the current paper and will be pursued in a future work.

IV. CONCLUDING REMARKS

We have investigated the local fluctuations of the internal structure and deformation in dense granular media based on DEM simulations. Numerical samples with different polydispersities are sheared under three-dimensional constant-volume condition and in the athermal quasistatic limit. Some key findings of the study are summarized as follows.

(1) The local structure of a granular medium can be characterized by an isotropic density and an anisotropic *fabric* defined from the Voronoi tessellation. Under constant volume shear, the local density is found to follow a gamma or mixed-gamma distribution which remains almost unchanged during the shearing process. The compactivity—a temperaturelike state variable for jammed granular media—is hence constant too during the shearing. However, this temperaturelike variable is found not in equilibrium among different particle groups within a polydisperse assembly.

(2) The distribution of local structural anisotropy can also be described by a gamma or mixed-gamma distribution which remains unaffected by the applied shearing. The global structural anisotropy of the whole assembly evolves significantly under shearing due to the change of local anisotropic orientation (i.e., rotation of the local Voronoi cell), which may change an initially isotropic (randomly distributed) assembly into a strongly anisotropic one (with preferred orientation). The structural anisotropy is also found coaxial with the applied stress anisotropy.

(3) The shear transformation zones identified from the local strain field are the plasticity carriers in a granular material. The development of STZs under shearing demonstrates clear evidence of the typical elastoplastic behavior of granular media. During the elastic regime, no STZs are observed, while at the sheared steady state STZs are found prevalent over the domain. The distribution of the local shear strain has a power-law decay at the tail part and its spatial correlation shows a long-range correlated characteristic which exhibits a

fourfold pattern in all three orthogonal cross sections. In the stress anisotropic planes, the particle flow is dominated by shearing effect and the correlation is much higher with longer range than that in the stress isotropic plane where the particle flow is more affected by thermal effect. The patterns indicate the isolated STZs in the granular sample play a similar role as that by the inclusions in an Eshelby elastic matrix.

(4) The pattern of the nonaffine displacement field is similar to that of the local shear strain, which suggests the two are intimately correlated and both can be used as plasticity measures. The distribution of the nonaffine displacements also has a power-law decayed tail. The distributions of the direction-decomposed nonaffine displacements at different shearing levels collapse to one single curve which can be well fitted with a q-Gaussian distribution function, showing an isotropic property of the slowly sheared granular temperature. This temperature remains unchanged under the applied constant-volume shearing. The spatial correlation of the nonaffine displacements remains long ranged, but shows an isotropic pattern in all three orthogonal cross sections, which differs from the local shear strain.

(5) The STZ model is modified to describe the pressure-dependent behavior of granular media. As the global volume is maintained constant in our study, the effective temperature is conserved during the shearing but the STZ formation energy increases due to the increase of confining pressure, which leads to a decreasing dimensionless effective temperature. By incorporating this dimensionless effective temperature as a state variable, the STZ model successfully predicts the evolution of the mean stress and the deviatoric stress in the simulated tests.

It is noteworthy that the modification of the STZ model in this study is a rather preliminary attempt. The evolution of pressure can be better accounted for by the so-called angoricity—another temperaturelike state variable defined in the stress ensemble [61,62] for a jammed granular medium. By taking into account both the compactivity and the angoricity as well as their coupled effects [63] in a constitutive model like the STZ, a unified general framework can be developed to model the evolutions of both volume and pressure, and to provide a

more comprehensive description of the behavior of granular media under more general and complex shearing modes, i.e., being complementary to the current constant-volume shearing, the constant-pressure tests can be investigated to shed light on the whole picture of the material behavior. Moreover, the anisotropy of local structures, seemingly less important in the spherical particle case, may play a major role affecting the overall behavior of granular media with complex-shaped particles [29,64], which needs further investigation.

[1] M. E. Cates, J. P. Wittmer, J.-P. Bouchaud, and P. Claudin, Phys. Rev. Lett. **81**, 1841 (1998).

[2] J. Zhang, T. S. Majmudar, M. Sperl, and R. P. Behringer, Soft Matter **6**, 2982 (2010).

[3] M. P. Ciamarra, M. Nicodemi, and A. Coniglio, Soft Matter **6**, 2871 (2010).

[4] A. J. Liu and S. R. Nagel, Nature (London) **396**, 21 (1998).

[5] S. F. Edwards and R. B. S. Oakeshott, Physica A **157**, 1080 (1989).

[6] T. Aste and T. DiMatteo, Phys. Rev. E **77**, 021309 (2008).

[7] K. Hernández and L. I. Reyes, Phys. Rev. E **77**, 062301 (2008).

[8] J. G. Puckett and K. E. Daniels, Phys. Rev. Lett. **110**, 058001 (2013).

[9] A. S. Argon, Acta Metall. **27**, 47 (1979).

[10] C. A. Schuh and A. C. Lund, Nat. Mater. **2**, 449 (2003).

[11] P. Schall, D. A. Weitz, and F. Spaepen, Science **318**, 1895 (2007).

[12] M. L. Falk and J. S. Langer, Phys. Rev. E **57**, 7192 (1998).

[13] E. Bouchbinder, J. S. Langer, and I. Procaccia, Phys. Rev. E **75**, 036107 (2007).

[14] E. Bouchbinder, J. S. Langer, and I. Procaccia, Phys. Rev. E **75**, 036108 (2007).

[15] J. S. Langer, Phys. Rev. E **77**, 021502 (2008).

[16] F. Radjai and S. Roux, Phys. Rev. Lett. **89**, 064302 (2002).

[17] C. Goldenberg, A. Tanguy, and J.-L. Barrat, Europhys. Lett. **80**, 16003 (2007).

[18] A. Tanguy, J. P. Wittmer, F. Leonforte, and J.-L. Barrat, Phys. Rev. B **66**, 174205 (2002).

[19] C. E. Maloney, Phys. Rev. Lett. **97**, 035503 (2006).

[20] G. Ovarlez, Q. Barral, and P. Coussot, Nat. Mater. **9**, 115 (2010).

[21] K. Wang, C. Song, P. Wang, and H. Makse, Europhys. Lett. **91**, 68001 (2010).

[22] K. Wang, C. Song, P. Wang, and H. A. Makse, Phys. Rev. E **86**, 011305 (2012).

[23] V. Chikkadi, G. Wegdam, D. Bonn, B. Nienhuis, and P. Schall, Phys. Rev. Lett. **107**, 198303 (2011).

[24] V. Chikkadi and P. Schall, Phys. Rev. E **85**, 031402 (2012).

[25] G. E. Schröder-Turk, W. Mickel, M. Schröter, G. W. Delaney, M. Saadatfar, T. J. Senden, K. Mecke, and T. Aste, Europhys. Lett. **90**, 34001 (2010).

[26] T. S. Majmudar and R. P. Behringer, Nature (London) **435**, 1079 (2005).

[27] D. Bi, J. Zhang, B. Chakraborty, and R. P. Behringer, Nature (London) **480**, 355 (2011).

[28] F. Radjai, D. E. Wolf, M. Jean, and J.-J. Moreau, Phys. Rev. Lett. **80**, 61 (1998).

[29] E. Azéma and F. Radjaï, Phys. Rev. E **85**, 031303 (2012).

[30] S. Abe, D. Place, and P. Mora, Pure Appl. Geophys. **161**, 2265 (2004).

[31] G. Goldenberg and I. Goldhirsch, Nature (London) **435**, 188 (2005).

[32] P. Jop, Y. Forterre, and O. Pouliquen, Nature (London) **441**, 727 (2006).

[33] N. Guo and J. Zhao, Comput. Geotech. **47**, 1 (2013).

[34] J. Zhao and N. Guo, Géotechnique **63**, 695 (2013).

[35] S. R. Williams, I. K. Snook, and W. van Megen, Phys. Rev. E **64**, 021506 (2001).

[36] V. Chikkadi, S. Mandal, B. Nienhuis, D. Raabe, F. Varnik, and P. Schall, Europhys. Lett. **100**, 56001 (2012).

[37] J. Christoffersen, M. M. Mehrabadi, and S. Nemat-Nasser, J. Appl. Mech. **48**, 339 (1981).

[38] M. J. Demkowicz and A. S. Argon, Phys. Rev. Lett. **93**, 025505 (2004).

[39] M. J. Demkowicz and A. S. Argon, Phys. Rev. B **72**, 245205 (2005).

[40] M. J. Demkowicz and A. S. Argon, Phys. Rev. B **72**, 245206 (2005).

[41] C. H. Rycroft, Chaos **19**, 041111 (2009).

[42] G. E. Schröder-Turk, W. Mickel, S. C. Kapfer, M. A. Klatt, F. M. Schaller, M. J. F. Hoffmann, N. Kleppmann, P. Armstrong, A. Inayat, D. Hug, M. Reichelsdorfer, W. Peukert, W. Schwieger, and K. Mecke, Adv. Mater. **23**, 2535 (2011).

[43] T. Aste, T. DiMatteo, M. Saadatfar, T. J. Senden, M. Schröter, and H. L. Swinney, Europhys. Lett. **79**, 24003 (2007).

[44] The fitting is performed using the mixdist package by the method of maximum likelihood estimation. P. Macdonald, with contributions from J. Du, mixdist: Finite Mixture Distribution Models, 2012, http://CRAN.R-project.org/package=mixdist.

[45] H. A. Makse and J. Kurchan, Nature (London) **415**, 614 (2002).

[46] M. Oda, H. Kazama, and J. Konishi, Mech. Mater. **28**, 103 (1998).

[47] H. Ouadfel and L. Rothenburg, Mech. Mater. **33**, 201 (2001).

[48] M. Satake, *IUTAM Symposium on Deformation and Failure of Granular Materials* (A. A. Balkema, Delft, 1982), pp. 63–68.

[49] M.-C. Miguel, A. Vespignani, S. Zapperi, J. Weiss, and J.-R. Grasso, Nature (London) **410**, 667 (2001).

[50] D. M. Dimiduk, C. Woodward, R. LeSar, and M. D. Uchic, Science **312**, 1188 (2006).

[51] J. D. Eshelby, Proc. R. Soc. London, Ser. A **241**, 376 (1957).

[52] G. Picard, A. Ajdari, F. Lequeux, and L. Bocquet, Eur. Phys. J. E **15**, 371 (2004).

[53] D. van der Meer and P. Reimann, Europhys. Lett. **74**, 384 (2006).

[54] L. G. Moyano, C. Tsallis, and M. Gell-Mann, Europhys. Lett. **73**, 813 (2006).

[55] A. Pluchino, A. Rapisarda, and C. Tsallis, Europhys. Lett. **80**, 26002 (2007).

[56] P. Jop, Y. Forterre, and O. Pouliquen, J. Fluid Mech. **541**, 167 (2005).

[57] G. D. R. MiDi, Eur. Phys. J. E **14**, 341 (2004).

[58] P.-E. Peyneau and J.-N. Roux, Phys. Rev. E **78**, 011307 (2008).

[59] J. J. Drozd and C. Denniston, Phys. Rev. E **81**, 021305 (2010).

[60] A. Lemaître, Phys. Rev. Lett. **89**, 195503 (2002).

[61] S. F. Edwards, Physica A **353**, 114 (2005).

[62] R. Blumenfeld and S. F. Edwards, J. Phys. Chem. B **113**, 3981 (2009).

[63] R. Blumenfeld, J. F. Jordan, and S. F. Edwards, Phys. Rev. Lett. **109**, 238001 (2012).

[64] B. Saint-Cyr, J.-Y. Delenne, C. Voivret, F. Radjai, and P. Sornay, Phys. Rev. E **84**, 041302 (2011).